4. J. V. Matthews and L. E. Ovenden, *Arctic* **43**, 324 (1990).
5. E. Hultén, *Outline of the History of Arctic and Boreal Biota During the Quaternary Period* (Cramer, New York, 1937).
6. K. O. Hedberg, *Bot. J. Linn. Soc.* **109**, 377 (1992).
7. D. F. Murray, in *Evolution Today: Proceedings of the Second International Congress of Systematic and Evolutionary Biology*, G. E. Scudder and J. L. Reveal, Eds. (Hunt Institute for Botanical Documentation, Carnegie Mellon University, Pittsburgh, PA, 1981), pp. 11–20.
8. D. M. Hopkins, Ed., *The Bering Land Bridge* (Stanford Univ. Press, Stanford, CA, 1967).
9. B. Frenzel, *Science* **161**, 637 (1968).
10. M. Stenström and U. Molau, *Arct. Alp. Res.* **24**, 337 (1992).
11. E. Hultén and M. Fries, *Atlas of North European Vascular Plants* (Koeltz Scientific, Königstein, Germany, 1986).
12. D. A. Webb and R. J. Gornall, *Saxifrages of Europe: With Notes on African, American and Some Asiatic Species* (Helm, London, 1989).
13. D. E. Soltis, P. E. Soltis, B. D. Ness, *J. Hered.* **81**, 168 (1990).
14. Supplemental Web material is available at www.sciencemag.org/feature/data/1050967.shl.
15. R. I. Milne, R. J. Abbott, K. Wolff, D. F. Chamberlain, *Am. J. Bot.* **86**, 1776 (1999).
16. R. J. Abbott, H. M. Chapman, R. M. M. Crawford, D. G. Forbes, *Mol. Ecol.* **4**, 199 (1995).
17. All samples were surveyed for restriction site variation using four enzyme:probe combinations (Bcl 1 × MB3, MB7; Eco R1 × MB3, MB7) (MB, mung bean), which, in a preliminary analysis, resolved considerable cpDNA variation in the species. These combinations distinguished all cpDNA haplotypes detected in the study, except K from L. Several individuals of each haplotype, sampled from throughout the geographical distribution of a haplotype, were further examined to determine the number of restriction site and indel differences among haplotypes over an additional 45 enzyme:probe combinations (Alu 1 × MB3, 7, 12; Bam H1 × MB3, 7; Bcl 1 × MB5+6; Bgl 2 × MB3, 7, 12; Cfo 1 × MB3, 5+6, 12; Cla 1 × MB3, 5+6, 7; Dra 1 × MB2, 3, 5+6, 7, 12; Eco R1 × MB5+6, 12; Hae 3 × MB2, 3, 5+6, 7, 12; Hinf 1 × MB3, 5+6, 7; Hpa 2 × MB1, 2, 3, 5+6, 7, 12; Rsa 1 × 3, 7; Sac 1 × MB3, 5+6, 7; Sal 1 × MB3, 7; and Pvu 2 × MB3, 7). In so doing, haplotype K was distinguished from L by a single site mutation.
18. D. L. Swofford, *PAUP: Phylogenetic Analysis Using Parsimony, Version 4.0b* (Sinauer, Sunderland, MA, 1998). Maximum parsimony trees were obtained with Wagner parsimony and involved a heuristic search with tree bisection-reconnection branch swapping, STEEPEST DESCENT off, MULTREES on, and ACCTRAN on. The robustness of trees was assessed by bootstrap percentages (after 1000 replications) and Bremer indices.
19. E. Hultén, *Bot. Not.* **126**, 459 (1973).
20. R. J. Gornall, unpublished data.
21. L. C. Cwynar, *Ecol. Monogr.* **52**, 1 (1982).
22. N. O. Tremblay and D. J. Schoen, *Mol. Ecol.* **8**, 1187 (1999).
23. H. P. Comes and J. W. Kadereit, *Trends Plant Sci.* **3**, 432 (1998).
24. G. M. Hewitt, *Biol. J. Linn. Soc.* **68**, 87 (1999).
25. J. I. Svendsen *et al.*, *Boreas* **28**, 234 (1999).
26. H. H. Birks, *Diss. Bot.* **234**, 129 (1994).
27. J. C. Ritchie, *Acta. Bot. Fenn.* **144**, 81 (1992).
28. T. M. Gabrielsen, K. Bachmann, K. S. Jakobsen, C. Brochmann, *Mol. Ecol.* **6**, 831 (1997).
29. K. J. Willis and R. J. Whittaker, *Science* **287**, 1406 (2000).
30. O. Pons and R. J. Petit, *Theor. Appl. Genet.* **90**, 462 (1995).

31. We thank the many colleagues who supplied us with plant material for analysis, especially F. Bretagnolle, C. Brochmann, T. Gabrielsen, U. Malm, and M. Stenström. The work was supported by a grant from the UK Natural Environment Research Council Special Topic Programme in Arctic Terrestrial Ecology (R.J.A and R.M.M.C).

3 April 2000; accepted 11 July 2000

Structure of Yeast Poly(A) Polymerase Alone and in Complex with 3′-dATP

Joel Bard,[1] Alexander M. Zhelkovsky,[2] Steffen Helmling,[2] Thomas N. Earnest,[3] Claire L. Moore,[2] Andrew Bohm[1,4]*

Polyadenylate [poly(A)] polymerase (PAP) catalyzes the addition of a polyadenosine tail to almost all eukaryotic messenger RNAs (mRNAs). The crystal structure of the PAP from *Saccharomyces cerevisiae* (Pap1) has been solved to 2.6 angstroms, both alone and in complex with 3′-deoxyadenosine triphosphate (3′-dATP). Like other nucleic acid polymerases, Pap1 is composed of three domains that encircle the active site. The arrangement of these domains, however, is quite different from that seen in polymerases that use a template to select and position their incoming nucleotides. The first two domains are functionally analogous to polymerase palm and fingers domains. The third domain is attached to the fingers domain and is known to interact with the single-stranded RNA primer. In the nucleotide complex, two molecules of 3′-dATP are bound to Pap1. One occupies the position of the incoming base, prior to its addition to the mRNA chain. The other is believed to occupy the position of the 3′ end of the mRNA primer.

Polyadenylation provides a universal handle by which transport and translation machinery can recognize and physically manipulate mRNAs. In eukaryotic organisms, addition of the poly(A) tail facilitates the transport of mRNA from the nucleus (*1*) and helps regulate mRNA stability (*2*). Interactions between proteins bound to the poly(A) tail and the 5′ end of mRNA in the cytoplasm are thought to cause circularization of the message and increase the efficiency of translation (*3*). Polyadenylation of mRNA is also observed in prokaryotes and appears to facilitate mRNA degradation (*4*).

Poly(A) tails are formed by a multiprotein complex which recognizes a polyadenylation signal at the 3′ end of a nascent transcript and cleaves the precursor RNA. PAP then adds the poly(A) tail [reviewed in (*5*)]. PAPs are well conserved across phyla with the first ~400 amino acids showing considerable sequence identity (*6*). The catalytic function of PAP resides in its NH$_2$-terminal domain (*7*), which shows sequence similarity to members of the nucleotidyl transferase (NT) family that includes DNA polymerase β (Polβ), CCA-adding enzymes, and several bacterial antibiotic resistance enzymes (*8*). Pap1 retains polymerase activity when separated from the holoenzyme assembly and can processively add long stretches of adenosine nucleotides to an RNA primer in vitro. Although it employs the same catalytic mechanism as other nucleic acid polymerases, PAP is significantly different in that it does not utilize a template strand to select and position the incoming nucleotide.

We have determined the the structure of both the apo and 3′-dATP–bound states of a Pap1 truncation mutant (Δ10PAP), which contains the NH$_2$-terminal 537 of the 568 amino acids in wild-type Pap1 (*9*). This truncated enzyme exhibits wild-type activity in vitro and is capable of rescuing an otherwise lethal disruption of the yeast PAP1 gene (*10*). Crystals formed from Δ10PAP contain two copies of Pap1 in the asymmetric unit cell (ASU). The structure was first solved to 3.2 Å by selenomethionine multiwavelength anomalous diffraction (MAD), and later refined against higher resolution data sets with and without 3′-dATP and divalent cations soaked into the crystals (Table 1) (*11*).

At first glance, Pap1 looks like many other polymerases. A large 20 Å by 30 Å by 45 Å cleft is bounded by three globular domains (Fig. 1). In other polymerases, this arrangement has been likened to a hand in which the substrates are held between the thumb and fingers and presented to an active site in the palm (Fig. 1, inset) (*12*). Pap1 differs from these polymerases, however, in that the

---

[1]Boston Biomedical Research Institute, 64 Grove Street, Watertown, MA 02472, USA. [2]Tufts University School of Medicine, Department of Molecular Microbiology, Boston, MA 02111, USA. [3]Macromolecular Crystallography Facility at the Advanced Light Source (ALS), Physical Biosciences Division, Lawrence Berkeley National Laboratory, Berkeley, CA 94720, USA. [4]Tufts University School of Medicine, Department of Biochemistry, Boston, MA 02111, USA.

*To whom correspondence should be addressed. E-mail: bohm@bbri.org

thumb domain is missing. The catalytic palm domain forms a wall of the cleft rather than sitting at its base. The base of the cleft interacts with the phosphates of the incoming nucleotide and is therefore functionally analogous to the fingers domains of other polymerases (*13*). The COOH-terminal domain forms the other wall of the cleft. Specificity determinants near the NH$_2$- and COOH-termini of Δ10PAP are known to interact with other components of the 3′ end processing machinery (*14*). These regions are on opposite sides of the structure, consistent with biochemical evidence that they function independently in regulating Pap1 activity.

The palm domain of Pap1 is structurally similar to the palms of other members of the NT family of proteins (*15, 16*). Three conserved acidic residues (aspartates 100, 102, and 154) coordinate the two metal ions required for catalysis. These metal ions and the incoming nucleotide are clearly visible in difference maps calculated using the native data and data from crystals soaked in 3′-dATP and either MgCl$_2$ or MnCl$_2$ (Fig. 2A) (*17*). The positions of the metal ions and phosphates correspond well with those observed in the active complex of Polβ (Fig. 2C) (*15*). Although the metals and phosphates exhibit very strong electron density, that of the ribose and base is weaker, suggesting that these parts of the substrate may be flexible (*18*).

We also observe electron density consistent with the presence of the sugar and base of a second 3′-dATP molecule (Fig. 2, A and B). Like that of the incoming nucleotide, the position of this density is very similar in both crystallographically independent copies of the complex. The second nucleotide occupies the position where the 3′ end of the primer would be expected based on the Polβ structure. The bases of the two nucleotides do not appear to stack, but are close enough to allow hydrogen bonding between N6 of the primer and N3 of the incoming nucleotide. This interaction does not, however, satisfactorily explain the selectivity of Pap1 for ATP as the incoming nucleotide (*14*). In other polymerases, formation of a correct base pair between the incoming nucleotide and the template is only detected in the "closed" conformation of the palm and fingers domains (*19*). It may be that Pap1 adopts a similar closed conformation during the catalytic cycle. Slight rotation of the fingers domain relative to the palm (see below) could place the conserved residue N226 within hydrogen bonding distance of the adenosine-specific N6 atom of the incoming nucleotide (*20*).

In contrast to the incoming nucleotide triphosphate, the mononucleotide primer shows extensive interactions with Pap1 (Fig. 2, D and E). The base of the primer 3′-dATP molecule stacks against the functionally important residue V141 (*21*). When the palm domains of Pap1 and Polβ are superimposed, Pap1 F140, which sits at the apex of the β-hairpin containing V141, occupies the same position as the +1 nucleotide of the Polβ template DNA. This β-hairpin may thus serve to compensate for the absence of a template in binding and positioning the primer. In addition, a hydrogen bond between the N6 amino group of the primer base and the main chain carbonyl of R186 could select for adenine over guanine.

The fingers domains of other polymerases

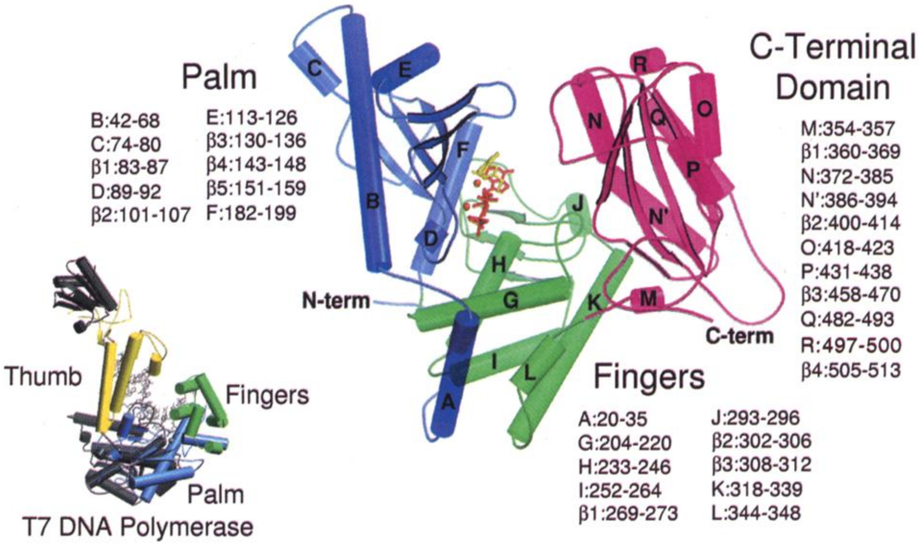

Fig. 1. Schematic view of Pap1. Residues 2 to 199 are shown in blue, 200 to 350 in green, and 351 to 530 in purple. The model is based on molecule B of the two independent copies of Pap1 in the ASU. Residues 445 to 456 and 473 to 478, which were not modeled in molecule B are based on the equivalent residues from molecule A. Two divalent cations (orange) are shown bound to the active site and to the phosphates of the incoming 3′-dATP (red). The mononucleotide primer is shown in yellow. The residues which form each secondary structure element are listed in a table adjacent to each subdomain. A model of T7 DNA polymerase [1T7P (*36*)] is shown in the inset for comparison. The color scheme for the palm and fingers domain is similar to that of Pap1. All figures were generated using three programs in sequence: MOLSCRIPT (*37*), R3D_TO_POV, and PovRAY.

Table 1. Crystallographic data and refinement statistics.

	Crystallographic data	
Space group (cell dimensions)	P2$_1$2$_1$2$_1$ (73.8 Å, 109.1 Å, 238.5 Å, 90°, 90°, 90°)	
Molecules per ASU	2 (537 amino acids per molecule)	
Solvent content*	70.0% (V_M = 4.11)	
	Structure determination (of the apo enzyme)	
X-ray source	ALS beamline 5.0.2	
Number of methionines/ASU	16 (8 in each molecule)	
Resolution	3.2 Å	
	Refinement statistics	
	Pap1 alone	Pap1 with 3′-dATP and Mn^{2+}
X-ray source	Rotating anode	SBC (APS beamline 19-ID)
Resolution limit	2.6 Å	2.6 Å
Observed (unique) reflections	141,762 (55,458)	242,159 (58,367)
% Complete (last shell)	92.6 (73.0)	97.8 (99.9)
R_{sym} (last shell)†	0.075 (0.314)	0.044 (0.397)
I/σ (last shell)	9.3 (2.9)	32.4 (2.8)
R_{work} (R_{free})‡	0.265 (0.298)	0.233 (0.279)
rms deviation from ideality		
Bond lengths	0.009	0.007
Bond angles	1.39	1.35
Dihedral angles	22.8	22.3
Water molecules modeled	112	83
Residues modeled		
Molecule A	3–427, 440–523	3–427, 440–523
Molecule B	2–444, 457–472, 479–530	2–444, 457–472, 479–530

*V_M = volume of the asymmetric unit/molecular weight of the protein scatterers. †$R_{sym} = \Sigma_{i,h}|I_{i,h} - \langle I_h \rangle|/\Sigma_{i,h}|I_{i,h}|$ where $\langle I_h \rangle$ is the mean of the *i* observations of the reflection *h*. ‡ $R_{work} = \Sigma||F_o| - |F_c||/\Sigma|F_o|$. R_{free} is the same statistic, but calculated for a subset of the data (10%) which had not been used during refinement. A 2σ cutoff was applied to the data during refinement.

rotate upon formation of the catalytic ternary complex with primer and NTP (*19*). Although we see no large-scale differences between the apo and the nucleotide-bound structures of Pap1, the two crystallographically independent molecules differ by ~5° in the orientation of the palm relative to the fingers. Interactions between the fingers domain and the incoming nucleotide are strongly affected by this rotation. In molecule B, Y224 and K215 are quite close to the incoming 3′-dATP, with the β-phosphate and K215 coordinating a water molecule (Fig. 2E). Molecule A, however, is in a more open conformation, and Y224 and K215 instead appear to interact with pyrophosphate (*22*), the by-product of the polymerase reaction (Fig. 2, A and D). K215 may therefore function to neutralize the pyrophosphate anion after catalysis. It has been proposed that similarly positioned lysines assume an analogous role in *Escherichia coli* DNA polymerase I (*23*) and T7 DNA polymerase (*24*).

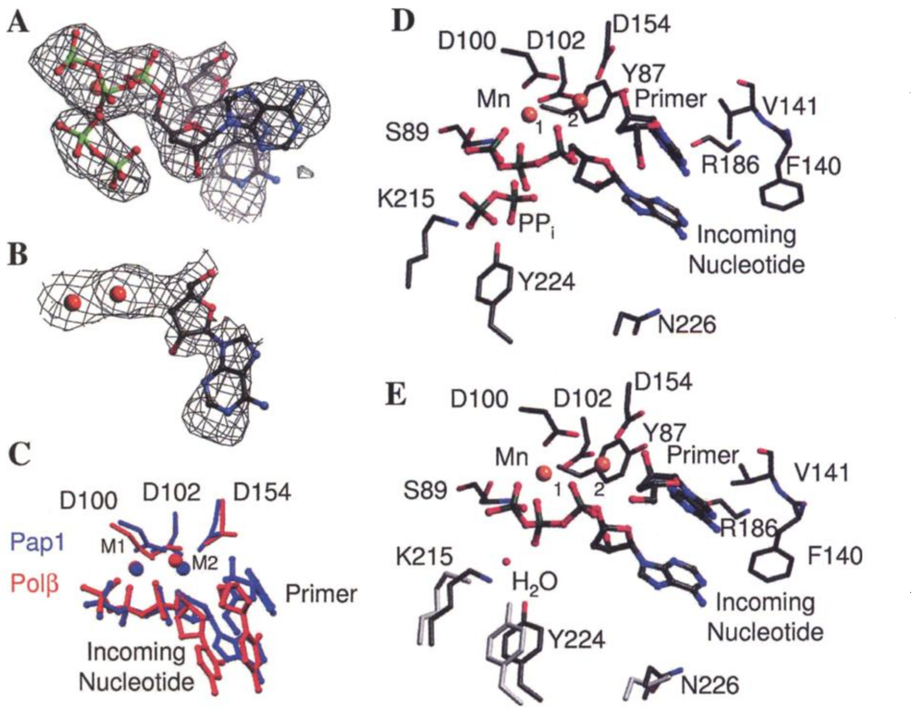

Fig. 2. Geometry of the active site. (**A**) $F_o - F_c$ simulated annealing omit map contoured at 2.5 σ showing electron density corresponding to the incoming 3′-dATP and PP$_i$ in molecule A. Additional density corresponding to the mononucleotide primer is visible in the background. Figure was prepared with BOBSCRIPT (*38*). (**B**) View of the electron density for the mononucleotide primer in the same map. Two Mn^{2+} atoms are shown in red. Only the adenine and ribose of this nucleotide are modeled. The phosphates were not visible in the electron density and are assumed to be disordered. (**C**) Superposition of the active sites of Pap1 (blue) and Polβ (red) [1BPY (*39*)] based on the side chains of the three catalytic aspartates. (**D**) Model of the active site from molecule A. (**E**) Model of the same region of molecule B. The positions of K215, Y224, and N226 in molecule A are shown in light gray for reference.

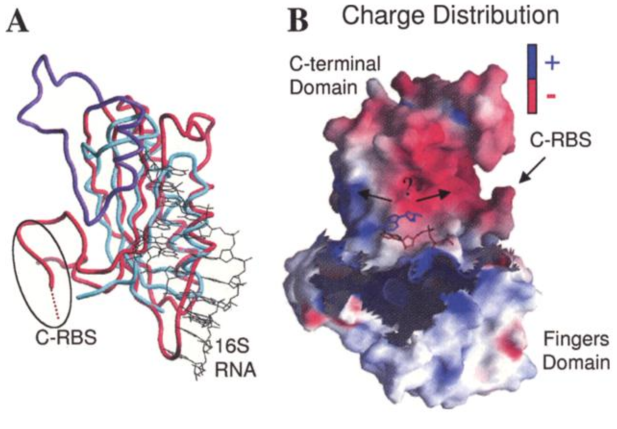

Fig. 3. (**A**) Superposition of ribosomal protein S6 from the core structure of the 30*S* ribosomal subunit [1EKC, cyan (*26*)] on the COOH-terminal domain of Pap1 (red). The portion of the 16*S* ribosomal RNA that interacts with S6 is shown in green. Residues 414 to 458 in Pap1, which have no equivalents in S6, are shown in purple. (**B**) The molecular surface of the fingers and COOH-terminal domains of Pap1 colored by charge distribution. The palm domain has been removed so that the inside of the cleft can be viewed from the vantage point of the active site. The incoming (red) and primer (blue) nucleotide positions are shown for reference. Amino acid residues in the C-RBS are to the right and behind the COOH-terminus in this view. The figure was prepared using the program GRASP (*40*).

The COOH-terminal domain of Pap1 binds the RNA primer/product. Residues 525 to 537 define a COOH-terminal RNA binding site (C-RBS) which is required for Pap1 processivity and for ultraviolet cross-linking to the upstream region of the RNA primer (*10, 14*). The C-RBS of Pap1 appears to be flexible, and we cannot model the electron density beyond residues 523 and 530 in molecules A and B, respectively (*25*). Those residues of the C-RBS which have been modeled extend away from the cleft, perhaps explaining why cross-linking to the Pap1 C-RBS is not observed when RNA is labeled only at its 3′ end (*10*).

There is considerable structural homology between the COOH-terminal domain and a number of nucleic acid binding proteins, including ribosomal protein S6 (*26*), and members of the RRM family of single-stranded RNA binding proteins (*27*). The strongest similarity was to S6 where the $C\alpha$ atoms of 70 residues may be superimposed with an rmsd of 2.5 Å (Fig. 3A). The face of S6 which binds the 16*S* RNA is analogous to the outside surface of Pap1, near the C-RBS. A group of conserved basic residues comprising K513 and a KKEK sequence in the loop preceding helix Q is also located in this region, suggesting that this part of the molecule may also play a role in RNA binding.

Although the shortest path between the active site and the C-RBS involves the RNA exiting the cleft from the front of the molecule (as viewed in Fig. 1), we have repeatedly observed weak electron density extending from the active site toward the rear of the cleft when short oligonucleotides are soaked into the crystals. A model in which the RNA exits from the rear of the cleft and wraps around to the C-RBS must therefore also be considered, particularly since the rear of the cleft is both more highly conserved and more basic than the front (Fig. 3B). Regardless of which path the RNA takes, binding of the poly(A) product to the inside face of the COOH-terminal domain could allow movements relative to the palm to disengage the RNA from the active site, as would be expected during translocation after addition of a new adenosine residue. Such movements of the COOH-terminal domain would occur as a result of the rotation of the attached fingers domain during catalysis. Additional binding at the C-RBS would then maintain processivity while allowing the translocated product to be released from the inside face of the COOH-terminal domain as the new 3′ end of the primer assumes its position for the next round of catalysis.

Note added in proof: Another group has recently determined the structure of the bovine poly(A) polymerase (*28*).

References and Notes

1. Y. Huang and G. C. Carmichael, *Mol. Cell. Biol.* **16**, 1534 (1996).
2. A. J. Carpousis, N. F. Vanzo, L. C. Raynal, *Trends Genet.* **15**, 24 (1999).
3. A. B. Sachs, P. Sarnow, M. W. Hentze, *Cell* **89**, 831 (1997).
4. G. A. Coburn and G. A. Mackie, *Prog. Nucleic Acid Res. Mol. Biol.* **62**, 55 (1999).
5. J. Zhao, L. Hyman, C. Moore, *Microbiol. Mol. Biol. Rev.* **63**, 405 (1999).
6. M. Ohnacker, L. Minvielle-Sebastia, W. Keller, *Nucleic Acids Res.* **24**, 2585 (1996).
7. G. Martin and W. Keller, *EMBO J.* **15**, 2593 (1996).
8. L. Holm and C. Sander, *Trends Biochem. Sci.* **20**, 345 (1995).
9. Untagged PAP was expressed and purified essentially as described (*10*), with the exception that the published heparin purification step was replaced with a Source S (Pharmacia) chromatography step. The peak fractions were concentrated to 40 mg/ml using a finger dialysis concentrator (Schleicher & Shuell, Keene, NH), exchanged into 75 mM NaCl, 10 mM sodium phosphate (pH 6.8), 2 mM $MgCl_2$, 1 mM dithiothreitol (DTT), and 20% glycerol and stored at −80°C, prior to crystallization. Typical yields of pure protein from this procedure were 1.2 mg/liter of *E. coli* culture for the full-length PAP, and 2.2 mg/liter culture for the Δ10 truncation. Selenomethionine was incorporated into the protein using an auxotrophic strain of *E. coli* into which the pLysS plasmid had been transformed and M9 growth media in which selenomethionine replaced methionine. The purification of the selenomethionine-incorporated protein was identical to that described above, however, the yield was significantly lower. PAP was crystallized at 4°C by vapor diffusion in hanging drops over wells containing 13.5% ethylene glycol, 9% PEG 8K, 6% glycerol, 100 mM Hepes (pH 7.24), and 2 mM DTT. The crystallization drops contained equal volumes of well solution and concentrated protein. Although full-length, bacterially-produced Pap1 is soluble to at least 35 mg/ml, it does not form crystals, and from dynamic light scattering measurements, it appears to be significantly aggregated. Crystals of Pap1 were initially grown using a 25–amino acid COOH-terminal deletion of the full length protein generated with endoproteinase Glu-C. The endoproteases Lys-C, thermolysin, and chymotrypsin produced similar fragments, suggesting that the COOH-terminus of Pap1 is intrinsically flexible. To improve the reproducibility of crystallization and quality of diffraction, data was collected from crystals formed from a previously characterized truncation of Pap1, Δ10PAP.
10. A. M. Zhelkovsky, M. M. Kessler, C. L. Moore, *J. Biol. Chem.* **270**, 26715 (1995).
11. MAD data (ALS, Berkeley, CA) was processed with MOSFLM and SCALA (*29*). Data from the Advanced Photon Source (Argonne, IL) beamline 19-ID was processed with HKL2000. Rotating anode data was processed with XDS (*30*). Eight of the 16 selenium positions were found by SOLVE (*31*), and the remaining sites were found by difference Fourier methods using solvent flattened phases derived from the initial selenium sites. Phase refinement was initially done using G. Van Duyne's GVX suite. Later, SHARP (*32*) was used to improve the quality of the selenomethionine MAD maps. The model was built using O (*33*) and refined using the simulated annealing torsion angle refinement protocol in CNS (*34*).
12. D. L. Ollis, P. Brick, R. Hamlin, N. G. Xuong, T. A. Steitz, *Nature* **313**, 762 (1985).
13. C. A. Brautigam and T. A. Steitz, *Curr. Opin. Struct. Biol.* **8**, 54 (1998).
14. A. Zhelkovsky, S. Helmling, C. Moore, *Mol. Cell. Biol.* **18**, 5942 (1998).
15. H. Pelletier, M. R. Sawaya, A. Kumar, S. H. Wilson, J. Kraut, *Science* **264**, 1891 (1994).
16. L. C. Pedersen, M. M. Benning, H. M. Holden, *Biochemistry* **34**, 13305 (1995).
17. Although PAPs are more active and less selective in the presence of Mn^{2+}, no significant differences between the $MgCl_2$- and $MnCl_2$-soaked crystals were seen at this resolution. The structure presented here has been refined against the $MnCl_2$ data because these data were of better quality. The identity of the manganese sites was confirmed by examining anomalous difference Fourier maps.
18. Initial difference Fourier maps were unclear about the orientation of the base. Refinement using a beta-version of BUSTER (*35*) showed the orientation of the base clearly. Subsequent refinement in CNS allowed unambiguous observation of the base in CNS simulated annealing omit maps.
19. S. Doublie, M. R. Sawaya, T. Ellenberger, *Struct. Folding Des.* **7**, R31 (1999).
20. The functional group of N226 is 4.4 Å away from N6 in the more closed copy of the complex, and 5.1 Å away from N6 in the more open copy of the complex.
21. Mutation of V141 to phenylalanine reduces the catalytic activity of Pap1 by more than 90% and causes a sixfold increases in the K_m for primer (A. M. Zhelkovsky, S. Helmling, C. L. Moore, unpublished data).
22. We believe that the pyrophosphate seen in the 3′-dATP soak was produced by a spurious reaction in which 3′-dATP was hydrolyzed to 3′-dAMP and inorganic pyrophosphate (PP_i). Data collected from crystals soaked in α-β-CH_2-ATP, a nonhydrolyzable ATP analog, do not show the pyrophosphate density.
23. L. S. Beese, J. M. Friedman, T. A. Steitz, *Biochemistry* **32**, 14095 (1993).
24. S. Doublie and T. Ellenberger, *Curr. Opin. Struct. Biol.* **8**, 704 (1998).
25. The proteolytic susceptibility of the C-RBS by endoproteinase Lys-C (A. Bohm, unpublished results) supports the notion that this region of the molecule may be intrinsically disordered.
26. S. C. Agalarov, G. Sridhar Prasad, P. M. Funke, C. D. Stout, J. R. Williamson, *Science* **288**, 107 (2000).
27. M. R. Conte *et al.*, *EMBO J.* **19**, 3132 (2000).
28. G. Martin, W. Keller, S. Doublie, *EMBO J.*, in press.
29. Collaborative Computational Project, *Acta Crystallogr. D* **50**, 760 (1994).
30. W. Kabsch, *J. Appl. Crystallogr.* **26**, 795 (1993).
31. T. C. Terwillinger and J. Berendzen, *Acta Crystallogr. D* **55**, 849 (1999).
32. E. de La Fortelle and G. Bricogne, *Methods Enzymol.* **276**, 472 (1997).
33. T. A. Jones, J. Y. Zou, S. W. Cowan, M. O. Kjeldgaard, *Acta Crystallogr. A* **47**, 110 (1991).
34. A. T. Brünger *et al.*, *Acta Crystallogr. D* **54**, 905 (1998).
35. G. Bricogne, *Methods Enzymol.* **276**, 361 (1997).
36. S. Doublie, S. Tabor, A. M. Long, C. C. Richardson, T. Ellenberger, *Nature* **391**, 251 (1998).
37. P. J. Kraulis, *J. Appl. Crystallogr.* **24**, 946 (1991).
38. BOBSCRIPT, version 2.4; R. Esnouf, Oxford University.
39. M. R. Sawaya, R. Prasad, S. H. Wilson, J. Kraut, H. Pelletier, *Biochemistry* **36**, 11205 (1997).
40. A. Nicholls, J. Bharadwaj, B. Honig, *Biophys. J.* **64**, 166 (1993).

41. We thank W. Somers for the use of computing facilities to run BUSTER and N. Duke, V. Srajer, and C. Ogata for their help collecting data. Also, we thank D. Jeruzalmi for his program R3D_TO_POV and for his help in interpreting the structure. This work was supported by NIH grant R01 GM57218-01A2 and American Cancer Society grant RPG-99-104-01-TBE. Coordinates for the complexed structure have been submitted to Protein Data Base (1FA0).

9 June 2000; accepted 13 July 2000

Differential Clustering of CD4 and CD3ζ During T Cell Recognition

Matthew F. Krummel,[1] Michael D. Sjaastad,[2] Christoph Wülfing,[1]* Mark M. Davis[1]†

Whereas T helper cells recognize peptide–major histocompatibility complex (MHC) class II complexes through their T cell receptors (TCRs), CD4 binds to an antigen-independent region of the MHC. Using green fluorescent protein–tagged chimeras and three-dimensional video microscopy, we show that CD4 and TCR-associated CD3ζ cluster in the interface coincident with increases in intracellular calcium. Signaling-, costimulation-, and cytoskeleton-dependent processes then stabilize CD3ζ in a single cluster at the center of the interface, while CD4 moves to the periphery. Thus, the CD4 coreceptor may serve primarily to "boost" recognition of ligand by the TCR and may not be required once activation has been initiated.

In higher vertebrates, T lymphocytes systematically scan cells and tissues for non-self antigens embedded in molecules of the MHC. Recognition of these peptide-MHC complexes is achieved through the αβ TCR, and signal transduction occurs through phosphorylation of the tightly associated CD3 γ, δ, ε, and ζ polypeptides (*1*). Several receptors on T cells can potentiate the response of the T cell, and their engagement is often required for successful activation in vivo. One of these is CD4 on T helper cells, which binds to relatively invariant sites on MHC class II molecules outside the peptide-binding groove (*2*, *3*) and accumulates at the T cell–antigen-presenting cell (APC) interface (*4*). During activation, CD4 increases T

---

[1] Department of Microbiology and Immunology, Stanford University School of Medicine, and the Howard Hughes Medical Institute, Stanford, CA 94305, USA. [2] Universal Imaging Corporation, 502 Brandywine Parkway, West Chester, PA 19380, USA.

*Present address: Center for Immunology, University of Texas Southwestern Medical Center, 5323 Harry Hines Boulevard, Dallas, TX 75390–9093, USA.

†To whom correspondence should be addressed: E-mail: mdavis@cmgm.stanford.edu